ARTICLES
PUBLISHED ONLINE: 29 APRIL 2012 | DOI: 10.1038/NMAT3307
nature materials

Atomically controlled electrochemical nucleation at superionic solid electrolyte surfaces

Ilia Valov[1]*, Ina Sapezanskaia[2], Alpana Nayak[3], Tohru Tsuruoka[3], Thomas Bredow[4], Tsuyoshi Hasegawa[3], Georgi Staikov[1], Masakazu Aono[3] and Rainer Waser[1,2]

Electrochemical equilibrium and the transfer of mass and charge through interfaces at the atomic scale are of fundamental importance for the microscopic understanding of elementary physicochemical processes. Approaching atomic dimensions, phase instabilities and instrumentation limits restrict the resolution. Here we show an ultimate lateral, mass and charge resolution during electrochemical Ag phase formation at the surface of $RbAg_4I_5$ superionic conductor thin films. We found that a small amount of electron donors in the solid electrolyte enables scanning tunnelling microscope measurements and atomically resolved imaging. We demonstrate that Ag critical nucleus formation is rate limiting. The Gibbs energy of this process takes discrete values and the number of atoms of the critical nucleus remains constant over a large range of applied potentials. Our approach is crucial to elucidate the mechanism of atomic switches and highlights the possibility of extending this method to a variety of other electrochemical systems.

The ability to control the physicochemical properties of surfaces at the atomic scale is of primary interest for a wide range of fields, including energy conversion, nanoelectronics and information technology, and nanoionics[1,2].

An electrochemically formed new phase consisting of a few to some tens of atoms in contact with a foreign substrate is expected to be thermodynamically unstable (as far as it can be physically defined as a phase). The charge, transferred in the elementary act(s), cannot exceed these tens of electrons, which is beyond the sensitivity limits of modern instrumentation. An uncertainty is also introduced by the fact that the well-defined macroscopic quantities are averaged and even single-crystalline substrates show local structural defects leading to microscopic inhomogeneities of the material properties. Therefore, the atomically resolved measurements of electrochemical processes require: a high precision in detecting mass and charge flow; a stabilization of thermodynamically metastable clusters of few atoms; and a knowledge of the local atomic structure and topography.

Despite the fact that the scanning tunnelling microscope (STM) provides atomic resolution and the ability to electrically manipulate surfaces, no reports can be found on measurements of superionic conducting solid electrolytes. The reason is the poor electronic conductivity of this class of materials suppressing the quantum mechanical tunnelling required by the STM. However, mixed electronic and ionic conducting solids with prevailing electronic conductivity ($\sigma_e \geq 10^3\sigma_{ion}$) were the subject of STM experiments and led to the development of the concept of the atomic switch demonstrating the ultimate scalability of the cation-based resistive switching memories[3,4] and the memristive systems[5].

The atomic switch is based on the electrochemical surface reaction of formation and dissolution, respectively, of nanosized metallic clusters of Ag or Cu on applying a short voltage pulse in the vacuum gap between the STM tip and a mixed electronic/ionic conducting solid, for example $Ag_{2+\delta}S$ and $Cu_{2+\delta}S$. Following its introduction[6], this technique was further developed to manipulate the resistance in the tunnel gap, where attempts have been made to elucidate the mechanism of the atomic switch[7–10].

The kinetics of the electrochemical formation of the small cluster (new phase) can be limited by the electron charge transfer or by the statistical process of (re)arrangement of the deposited atoms in an energetically stable configuration, that is, the formation of the critical nucleus. If the number of atoms (N_c) constituting the critical nucleus is lower than approximately 20, the thermodynamics and kinetics of the cluster are given by the atomistic theory of nucleation, accounting for the discrete character of the system[11–13].

Once formed, the nucleus may further grow, establishing a single atomic contact to the STM tip. This mechanical contact thermodynamically stabilizes the cluster. Knowledge of the tip–sample distance enables estimation of the number of atoms in the cluster, the partial charge used in the redox process and the Faraday efficiency.

Thin films of 150 nm $RbAg_4I_5$ thermally evaporated on 500 nm Ag films deposited on platinized Si wafer substrates were investigated by the STM technique. The choice of $RbAg_4I_5$ as a model system was justified by the well-known defect structure and transport properties of this material and the demonstrated superionic conductivity at room temperature (Supplementary Section S7). The STM imaging and spectroscopy were crucial prerequisites to calibrate the tip–sample distance and to observe and visualize the surface structure and morphology before and after the electrochemical formation and dissolution of Ag clusters. To enable the measurements, we used $RbAg_4I_5$ doped with a small amount of Fe (0.1 at.%). Density functional theory (DFT) calculations showed that irrespective of their particular site position in the cation sublattice, Fe dopant atoms induced new occupied levels approximately 1 eV below the conduction band, contributing to the increase of the electronic partial conductivity (Supplementary Fig. S5). Thus, the crystallographic structure and the superionic

[1]Research Centre Juelich, Peter Gruenberg Institute, Electronic Materials, 52425 Juelich, Germany, [2]IWE2 & JARA-FIT, RWTH Aachen University, 52056 Aachen, Germany, [3]International Center for Materials Nanoarchitectonics (WPI—MANA), National Institute for Materials Science (NIMS), 1-1 Namiki, Tsukuba 305-0044, Japan, [4]Institute of Theoretical Chemistry, University of Bonn, 53115 Bonn, Germany. *e-mail: i.valov@fz-juelich.de.

properties were preserved, that is, the transference number of the ions is $t_{ion} > 0.99$, but an electronic conductivity of the order of $\sigma_e = (10^{-2} - 10^{-3})\sigma_{ion}$ (measured by the Hebb–Wagner polarization technique[14,15]) was sufficient for quantum mechanical tunnelling (Supplementary Fig. S4).

In the STM tip–tunnel gap–(Ag)$RbAg_4I_5$–Ag system, we define, on a microscopic level, three boundary states qualitatively describing the initial, an intermediate and the final stages before and after the formation of the metallic Ag cluster in the tunnel gap. These states account for the creation and disappearance of new interfaces and the corresponding change in the distribution of the potentials, as illustrated by the physical model in Fig. 1.

Approaching a tunnelling distance, the Fermi level of electrons of the STM tip and the sample, or their electrochemical potentials $\tilde{\mu}_e$(tip), $\tilde{\mu}_e$(Ag), equilibrate and the condition E_F(tip) = E_F(Ag) or, respectively, $\tilde{\mu}_e$(tip) = $\tilde{\mu}_e$(Ag) is fulfilled presuming no net current flow.

The main potential drop is concentrated between the STM tip and $RbAg_4I_5$ (Fig. 1a). The electric potential gradients in the solid electrolyte and at the $RbAg_4I_5$/Ag interface can be practically neglected. The physical model for an electrical double layer in electrochemical systems[16] can be applied considering the tunnel gap as an extended Helmholtz (dense) part. Thus, the voltage applied between the STM tip and the Ag electrode equals the voltage drop between the STM tip/vacuum and the vacuum/$RbAg_4I_5$ interfaces; that is, φ(tip/vacuum) − φ(vacuum/$RbAg_4I_5$) = $\Delta\varphi$. This is strictly valid in the initial stages when either no or only very few Ag atoms are deposited.

An applied voltage shifts the Fermi level of the STM tip relative to the sample (ΔE_F(tip) = $-e\Delta\varphi$) and an effective tunnelling current is induced.

Electrons arriving at the $RbAg_4I_5$ surface with an energy lower than the Fermi energy of the redox reaction (1), that is, $E_F < E_F(Ag^+/Ag)$, can only tunnel but cannot contribute to the electrochemical reaction. After achieving the energy level of $E_F > E_F(Ag^+/Ag)$, the tunnel electrons can overcome the energy barrier for the Ag^+/Ag redox reaction.

$$Ag^+ + e^- \rightleftharpoons Ag \qquad (1)$$

Assuming elastic tunnelling, the application of a potential difference $-\Delta\varphi$, that is, $E_F(\text{tip}) + e\Delta\varphi > E_F(Ag^+/Ag)$, will shift the equilibrium of reaction (1) to the right; that is, atomic Ag will be deposited at the vacuum/$RbAg_4I_5$ interface. Keeping the electroneutrality at the $RbAg_4I_5$/Ag interface, an equal amount of Ag will be oxidized entering the $RbAg_4I_5$. Here we take into account that the chemical potential μ_{Ag} at the interface $RbAg_4I_5$/Ag is thermodynamically fixed and reaction (1) is reversible and, therefore, the Ag electrode is considered as non-polarizable. Another factor ensuring negligible polarization is the much larger surface area of the Ag electrode when compared with the working electrode area (STM tip).

Thus, at $E_F < E_F(Ag^+/Ag)$ we performed the STM imaging and at $E_F > E_F(Ag^+/Ag)$ we performed electrochemical measurements of the reaction kinetics.

Figure 2 shows atomically resolved STM images of a superionic solid electrolyte.

The STM images depict the (110) face, complementing the X-ray diffraction (XRD) measurements showing the strongest signal for the (110) reflection (Supplementary Fig. S3) and, in particular, revealing the absence of any surface reconstructions. The deviations from the reported lattice parameters are on average less than 5% but for different samples we also observed up to 15% deviation. We relate it to thermal and/or vibration shifts, which are, however, not surprising for STM measurements at room temperature.

Next, the initial stages of Ag cluster formation were studied by applying a negative voltage to the STM tip fulfilling the

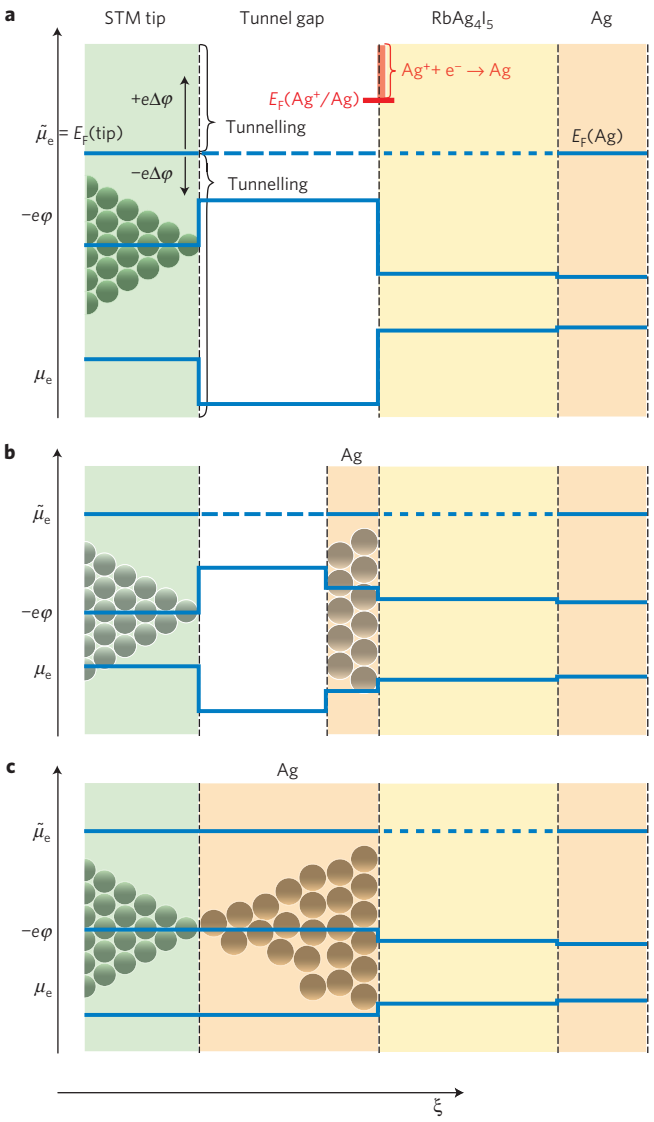

Figure 1 | Schematic presentation of the distribution of the electrochemical ($\tilde{\mu}_e$), chemical (μ_e) and electrical (φ) potentials (related by $\tilde{\mu}_e = \mu_e - ze\varphi$) at three boundary situations. a, Equilibrium for the initial state of the system. The vertical arrows indicate the shift of the equilibrium and the induced processes when a voltage is applied. **b**, After the formation of the Ag nucleus at the $RbAg_4I_5$ interface (two new contact interfaces are present—vacuum/Ag and Ag/$RbAg_4I_5$). **c**, After the mechanical contact between the metallic filament and the STM tip (the interfaces STM tip/vacuum and vacuum/Ag disappeared).

condition $E_F(\text{tip}) + e\Delta\varphi > E_F(Ag^+/Ag)$. Owing to the specifics of the system, no steady-state measurements can be performed, but rather short-voltage-pulse experiments. On applying a negative voltage pulse, a switching event occurs (short-circuiting the vacuum gap) in times ranging between some milliseconds and nanoseconds, with switching times t_s being exponentially dependent on the value of the applied potential.

In Fig. 3 the current–time dependence is shown by applying a cathodic voltage pulse.

Five regions were distinguished. In region (1), at a constant voltage of +100 mV, a current of 1 nA (in tunnelling current modus) was set to avoid deposition of Ag atoms at the surface. In region (2), after applying the negative voltage pulse of −100 mV, first the current rapidly changes to a value of −0.8 nA and then decreases slightly. No Faradaic reaction occurs. In region

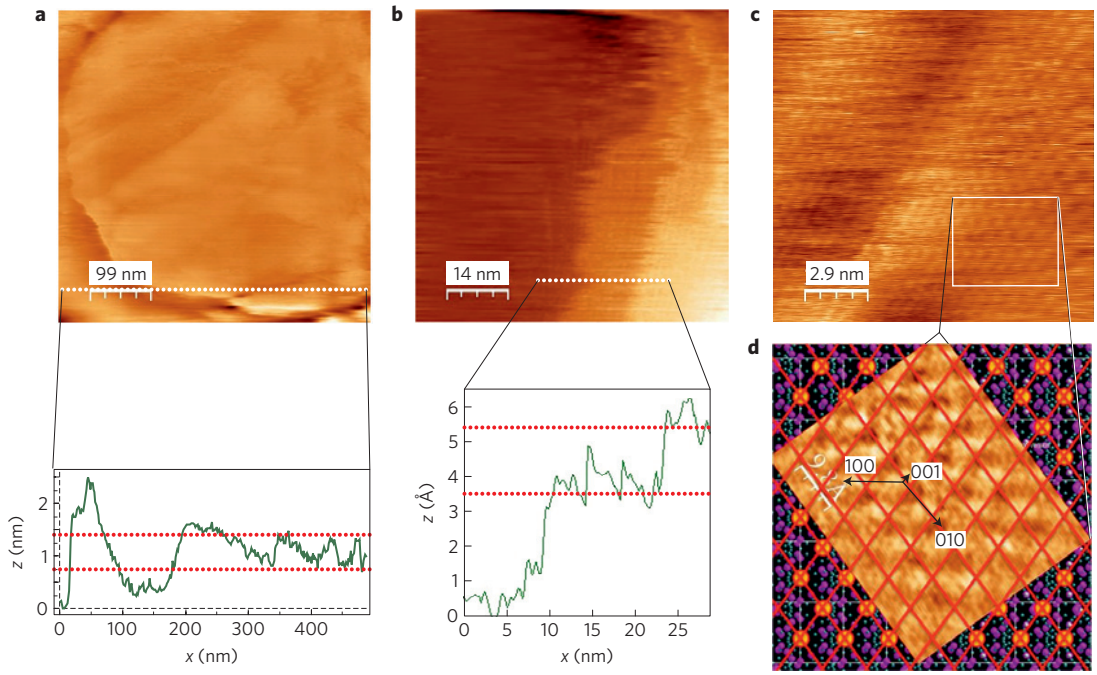

Figure 2 | STM imaging of $RbAg_4I_5$ surfaces. a,**b**, STM images of a $RbAg_4I_5$ grain (**a**), and monatomic steps (**b**) with the corresponding (*x*-*z*) profiles. **c**,**d**, Atomically resolved (110) face. The brighter spots show the I^- ions. The images were recorded using a set-point tunnelling current of 1 nA at tunnelling voltages of 50 mV, 75 mV and 75 mV for images **a**, **b** and **c**, respectively (below the decomposition voltage of $RbAg_4I_5$). Further STM images are shown in Supplementary Fig. S7.

(3), a Ag filament starts forming and the current rises abruptly. In region (4), the filament short-circuits the tunnel gap and the conductivity reaches the value for a single-point quantum conductance $G_0 = 2e^2/h$. The filament becomes larger, the current increases and additional quantum steps can be observed. In region (5), the filament broadens, further reducing the resistance, and finally the current reaches its maximum value limited by an external reference resistor of 10 kΩ.

The switching time t_s, that is, the time between applying the voltage pulse and the time of achieving the single quantum contact, is defined as the time difference $t_s = t_4 - t_2 = t_n + t_g$, with $t_n = t_3 - t_2$ being the nucleation time and $t_g = t_4 - t_3$ being the time of nucleus growth. From Fig. 3 it can be clearly seen that the main contribution to t_s is that of region (2) whereas the influence of region (3) is negligible; that is, $t_s \sim t_n$. Applying more negative voltages down to −600 mV and/or higher temperatures results in shortening of the time t_n but no detectable influence of those two factors on the time t_g was observed.

We unequivocally relate the short-circuiting of the tunnel gap to a formation of a Ag nucleus induced by the electrochemical reaction given by equation (1). The elementary steps of formation of one or few Ag atoms at the $RbAg_4I_5$ surface represents an electrochemical reaction limited by the initial stage(s) of formation of a new phase (Ag) on a foreign substrate, that is, the nucleation. The nucleation rate J(s) is given in accordance to the atomistic model for electrocrystallization, for applied cathodic potentials ($\Delta\varphi < 0$) higher than kT/e by:

$$J = \underbrace{N_{Ag^+} Z_0 \Gamma \aleph \frac{kT}{h} \exp\left(-\frac{\Delta G^{\neq} + \Phi(N_c)}{kT}\right)}_{J_0} \exp\left(-\frac{(N_c + \alpha) e \Delta\varphi}{kT}\right) \quad (2)$$

where N_{Ag+} and Z_0 are the numbers of Ag^+ ions and of active sites, respectively, which in the case of STM analysis can take a value of unity; Γ is the Zeldovich factor, which tends to unity for small clusters and high cathodic $\Delta\varphi$; ℵ is the transmission probability of an electron; h is the Planck constant; $\Delta G^{\neq}$ is the free activation enthalpy of the charge transfer reaction (at $\Delta\varphi = 0$), $\Phi(N_c)$ is the specific surface energy of the critical nucleus and α is the cathodic transfer coefficient. The pre-exponential term marked by J_0 (nuclei/s) is constant at given constant thermodynamic conditions and it changes only if the number of atoms of the critical nucleus or the charge transfer mechanism changes (Supplementary Section S1). The nucleation rate–voltage dependence given in logarithmic coordinates ln J versus $\Delta\varphi$ has a similar form to the Tafel dependence and is used to calculate the parameter N_c. In the lower limit boundary condition, that is, $N_c = 0$, the slope of this dependence transforms to the classical Tafel slope derived from the Butler–Volmer equation[17,18]. We define the time required to create the critical nucleus as t_n (nucleation time). During t_n, atomic rearrangements take place until the atomic configuration with a minimum energy is reached. No net Faraday current flows during this process.

After the critical nucleus is stabilized, it starts growing. The growth rate is characterized by an abrupt increase of the current starting at time t_3. As evident from Fig. 1b, two new interfaces are introduced after the critical nucleus is formed. The potential drop and, hence, the current are determined by the contributions of both the tunnel gap and the electron charge transfer (given by the Butler–Volmer equation) dynamically changing with increasing nucleus size. After short-circuiting the tunnel gap by the Ag cluster (Fig. 1c), the potential drop is located at the interface Ag-cluster/$RbAg_4I_5$. The time for the growth process is given by t_g. Figure 3 indicates that t_g can be neglected and presuming $t_n \sim t_s$ the relation between t_s and $\Delta\varphi$ is derived from equation (3):

$$t_s = t_0 \exp\left(\frac{(N_c + \alpha) e \Delta\varphi}{kT}\right) \quad (3)$$

with $t_0 = 1/J_0$(s). For cathodic voltages, $\Delta\varphi$ takes negative values and the switching time decreases exponentially with increasing

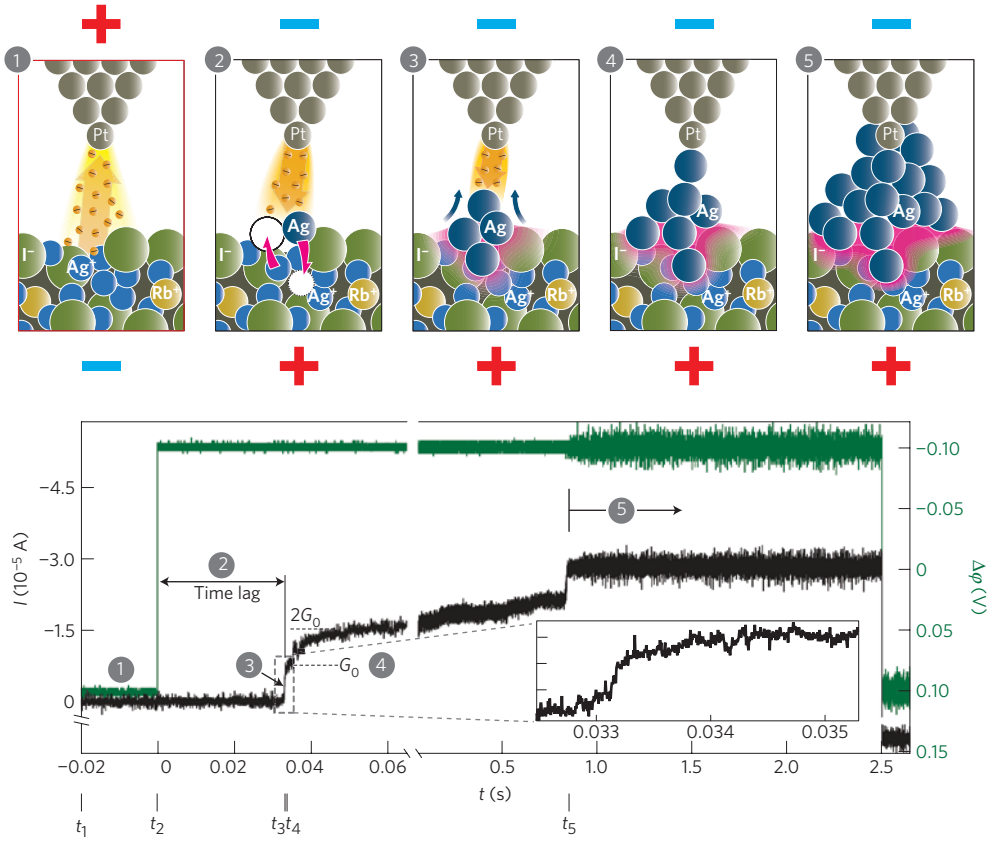

Figure 3 | Current–time dependence at an applied voltage of −100 mV. t_i ($i = 1$–5) denotes the starting time of the ith process step. The number (1–5) notation relates the 5 regions defined in the current–time characteristics to the microscopic model (upper part of the graph) for the sequence of individual physicochemical processes during the switching. Only 4 Ag atoms in a chain are sufficient to short-circuit a gap of 1 nm (typical tip–sample distance). Accounting for dispersion of the tunnelling current beam area up to 20 Ag atoms can be calculated to constitute a cluster of a conical or tetrahedral form. The inset shows the first quantum step at G_0. The sharpness of the current increase is determined by the rate of the filament growth. The I–t curve is exemplarily extracted from one of the data points shown in Fig. 4a.

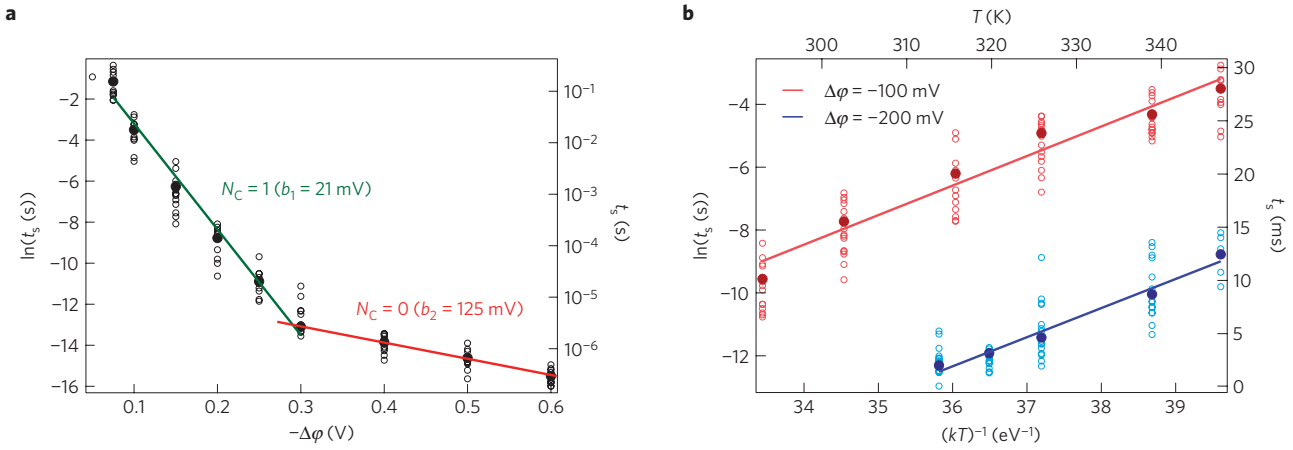

Figure 4 | Voltage and temperature dependence of the switching time. a,**b**, Dependence of the switching time t_s on the applied voltage for $T = 300$ K (**a**), and on the temperature at two constant voltages (**b**). As the nucleation is a stochastic event, a statistical dispersion of t_s values is expected. Every data point is extracted from an analysis such as the one shown in Fig. 3.

cathodic voltage. Figure 4a shows the switching time as a function of the applied voltage in semi-logarithmic coordinates.

Two linear regions can be distinguished—region 1 between −75 mV and −300 mV and region 2 between −300 mV and −600 mV. The corresponding reciprocal slopes were calculated to be $b_1 = 21$ mV and $b_2 = 125$ mV, and accounting for $kT/e = 25$ mV, the parameter $(N_c + \alpha)$ is estimated to be 1.25 and 0.2, respectively. To determine N_c, knowledge about α is required. The transfer coefficient α is generally defined as the change in the activation energy normalized to the applied potential difference, but also (as originally introduced[18]) it gives the geometrical position of the potential energy barrier maximum in the dense Helmholtz part of the electrical double layer. Thus, by varying the tip–sample distance d (the tunnel gap), we also change the geometrical position of the

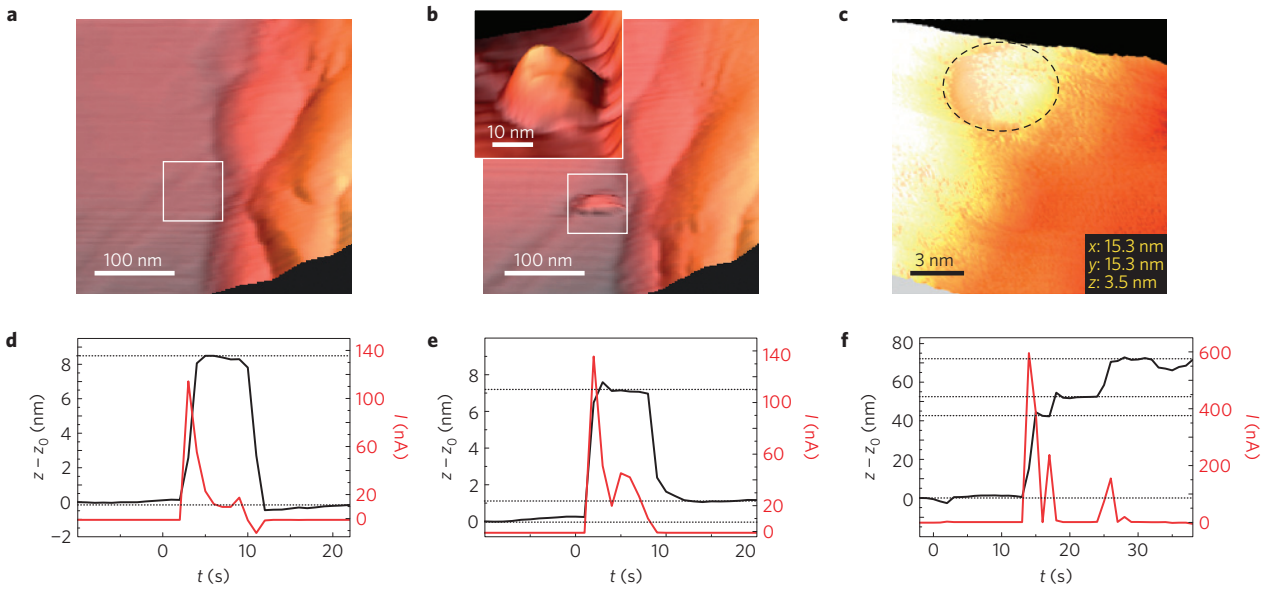

Figure 5 | STM observations of Ag clusters formation and stability. a,**b**, 3D STM imaging of $RbAg_4I_5$ surface before applying a voltage pulse (**a**) and after the cluster is formed (**b**). **c**, The smallest filament we were able to detect. **d**–**f**, Determination of the filament height by *I*–*z* measurements. In **d**, the pulse length was 10 ms ($\Delta\varphi = -250$ mV); for **e** the pulse length was the same but $\Delta\varphi = -350$ mV; and in **f** the pulse length was 50 ms. z_0 denotes the initial *z* position. The change in the current is associated with a *z* variation due to partial growth and dissolution of Ag (I_{tunnel} depends exponentially on the tip–sample distance).

potential energy maximum (for Ag^+/Ag reaction) and, therefore, the transfer coefficient α. It will vary and must be determined for each constant *d*.

To determine α we used the condition that in region 2 the applied cathodic potentials were sufficiently negative and we have achieved the condition $N_c = 0$ and, thus, the value for the transfer coefficient can be estimated: $\alpha = 0.2$. As we performed our experiments always at the same *d*, the value determined for α was further used in our calculations for different voltages. Thus, in region 1 we found $N_c = 1$ and in region 2 $N_c = 0$. $N_c = 1$ has the physical meaning that each atom of Ag created at the $RbAg_4I_5$ surface can be considered as a nucleus of the new phase and $N_c = 0$ means that an empty nucleation site acts as a critical nucleus and the single created Ag atom represents a supercritical cluster of the new phase.

The activation energy of the nucleation process can be obtained from the temperature dependence of the switching time from the slope $(\partial \ln t_s/\partial T)_{\Delta\varphi}$. In Fig. 4b the results at constant voltages of -100 mV and -200 mV are shown. The mean activation energy was found to be $\Delta G_a = (1.0 \pm 0.1)$ eV. This result proves, first, that the electrochemical barrier (nucleation) and not the tunnelling barrier controls the overall reaction rate and, second, it definitely excludes the diffusion of Ag^+ ions in the $RbAg_4I_5$ to be rate limiting, because this shows a very different value of approximately 0.12 eV (ref. 19). However, we should note that the determined energy barrier includes both terms—the charge transfer and the surface energy term given in the first pre-exponential factor of equation (2), respectively in equation (3).

To image clusters by STM analysis and determine their lifetime, pulses of different amplitudes were applied with a switched on feedback modus. Thus, by quickly withdrawing the tip, the clusters were not allowed to mechanically contact the STM tip (no switching event occurs). The deposited clusters (if stable) were imaged afterwards in a positive-voltage regime. In Fig. 5, images of the $RbAg_4I_5$ surface before and after the deposition of a stable cluster are shown.

No upper limit of the filament size was found, but there is a lower size limit determined by the thermodynamic stability of the Ag phase. The smallest cluster we succeeded to detect by STM imaging was approximately 5 nm in diameter and 3 nm in height (Fig. 5c). Stability of smaller clusters with a height of down to 1 nm was indicated by current–displacement (*I*–*z*) measurements shown in Fig. 5e. However, their long-term stability could not be confirmed by imaging.

Free-standing clusters below this size were unstable. We detected their formation and lifetime only by *I*–*z* measurements. Figure 5d shows the current (*z*) oscillations during the formation and a complete dissolution of metastable clusters. After the end of the pulse, the current value equals the value before the pulse; that is, no irreversible morphology change had occurred. For higher cathodic voltages, the clusters can be stabilized and a step-wise growth can be observed (Fig. 5e,f). Thus, we demonstrated free-standing clusters and observed their dynamics. The Faraday efficiency was estimated for both atomic switches and free-standing larger clusters using a conical (and tetrahedral shape) shape and the three-dimensional cluster volume as imaged by the STM, respectively. The Faraday current was 10^{-8} times lower than the total current of the pulse. We associate the low efficiency with the much lower energy barrier for the electron tunnelling, determined to be on average only 80 meV (Supplementary Fig. S6), in comparison with the barrier of the electrochemical process.

In this study we offer an alternative approach for studying electrochemical reactions on a microscopic level with an ultimate lateral, mass and charge resolution based on the atomic-switch concept. By increasing the electronic partial conductivity of $RbAg_4I_5$, we were able to use the STM technique on superionic conducting solids, which allowed for recording of an atomically resolved image of a solid electrolyte at room temperature. We demonstrate that the very initial stage of an electrochemically driven formation of a new phase is limited by the critical nucleus formation.

We suggest the possibility of extending our method to other solid- and liquid-based ionic conductors that are used in sensors, fuel cells and catalysts.

Methods

Thermal evaporation. We used platinized Si wafers as substrates to deposit our thin-film systems. First, the substrates were covered with 100 nm Ag by thermal evaporation. Then, 150 nm $RbAg_4I_5$ was deposited by evaporation from a mixture of

AgI and RbI in a ratio of AgI/RbI = 78:22. In the AgI powder, 0.1 at.% of Fe provided additional electronic states in the film. Alternatively, AgI, RbI and 0.1 at.% Fe were melted at 400 °C for 2 h in vacuum glass and then quenched and annealed at 160 °C for 15 h. The sample was milled, the crystal structure was controlled by XRD and the powder was used for thermal evaporation. No measurable difference in the electrical properties was observed, but the films prepared by co-evaporation showed a higher level of crystallinity. The thermal evaporation process was carried out in vacuum ($<10^{-3}$ Pa) at a substrate temperature of 70 °C and a deposition rate of 1 Å s^{-1} to ensure optimal conditions for homogeneous coverage and film crystallization. The thickness of the films was estimated by a quartz crystal microbalance.

Characterization. The $RbAg_4I_5$ film thicknesses were controlled by high-resolution scanning electron microscopy using a Zeiss DSM 982 Gemini at voltages between 1 kV and 20 kV; working distances of 2–3 mm and magnifications up to ×200,000 have been used.

XRD measurements were performed to confirm the structure of the deposited films with an X'Pert PRO PANalytical system from Phillips with CuKα1 irradiation ($\lambda = 1.5406$ nm). The assignment of the reflections was performed according to the JCPDS files: 03-0921, 74-1416, 83-0581, 83-1951, 01-0513, 73-0385, 44-0063, 02-0645 and 39-1159.

The ionic and electronic partial conductivities were determined using the Hebb–Wagner polarization technique with a Ag bottom electrode and Pt ion blocking electrodes with an area of 3×10^{-6} cm^2 deposited on the samples by a photolithographical process. The current–time measurements were performed as a function of the applied voltage with a Keithley 428 current source amplifier.

The STM experiments were carried out at 10^{-4} Pa using Pt tips for atomic-switch experiments and W tips for the imaging and current–displacement (I–z) spectroscopy. The Pt tips were sharpened with a focused ion beam and the W tips were etched in aqueous NaOH solution and subsequently properly rinsed in deionized water. Both the tips were cleaned by annealing in a vacuum chamber by holding the tip apex close over a glowing W wire. Constant-voltage pulses were applied using a pulse generator (NF WF1946) and the output signal was measured using a digital oscilloscope (Wave Runner 6100, LeCroy).

The switching experiments were started after a stable tunnelling contact between the STM tip and the sample was established at a positive tip potential of $\Delta\varphi = 50$ mV and a constant current of $I = 1$ nA unless stated otherwise. As soon as the drift stabilized, the tip–sample distance was fixed by switching the STM feedback control off. Subsequently, rectangular voltage pulses of opposite tip polarity between −50 mV and −600 mV and duration between 10–7 s and 1 s were applied. The data analysis performed on the basis of the I–t characteristics (as exemplarily shown in Fig. 3) accounts for the reference resistance of 10 kΩ.

The atomically resolved images were obtained at a tunnelling current of 1 nA, a sample bias voltage between 20 mV and 150 mV and a scanning speed rate between 200 nm s^{-1} and 1,000 nm s^{-1}. The non-atomically resolved images were processed by parabolic plane subtraction.

Quantum-chemical calculations. The accompanying quantum-chemical model calculations were performed with the crystalline-orbital program package CRYSTAL09 (ref. 20). On the basis of our experience with other systems, we applied the DFT–Hartree–Fock hybrid method PW1PW (ref. 21) for electronic structure calculations of Fe-doped and undoped $RbAg_4I_5$. The heavier elements Rb, Ag and I were described with quasi-relativistic Stuttgart-Dresden ECP28MWB effective core potentials[22–24] and slightly modified valence basis sets.

Fe was given a modified Def2-TZVP all-electron basis set[25].

In the crystallographic structure[26] with $Z = 4$, the Ag occupies Wyckoff positions 24e, 24e′, 8c and 4b with occupation numbers $f = 0.391, 0.229, 0.111, 0.084$. As the quantum-chemical models require a specific repeat unit with certain positions for all atoms, a pre-selection of realistic Ag distributions was performed in preliminary test calculations. It turned out that the most stable structure contains 8 Ag on site 24e ($f = 0.333$), 6 Ag on site 24e′ ($f = 0.250$), 1 Ag on site 8c ($f = 0.125$) and no Ag on site 4b, close to the experimental averages.

Fe doping was modelled by adding a neutral Fe atom to the lattice at one of the vacant Ag lattice sites. Four sites were taken into account, position 24e (0.2287.0.2020,0.0299), position 24e (−0.0036, −0.1494, 0.2154), position 8c (0.1739,0.1739,0.1739) and position 4b (0.125, 0.375, −0.375). The first three sites are energetically similar to PW1PW (within 10 kJ mol^{-1}), so that at this level of theory no distinction is possible. Only the 4b site leads to a significantly higher energy and is therefore excluded from the electronic structure calculations.

Received 23 August 2011; accepted 19 March 2012; published online 29 April 2012

References

1. Maier, J. Nanoionics: Ion transport and electrochemical storage in confined systems. *Nature Mater.* **4,** 805–815 (2005).
2. Waser, R. (ed.) *Nanotechnology—Volume 3, Information Technology* (Wiley, 2008).
3. Valov, I., Waser, R., Jameson, J. R. & Kozicki, M. N. Electrochemical metallization memories-fundamentals, applications, prospects. *Nanotechnology* **22,** 254003 (2011).
4. Waser, R. & Aono, M. Nanoionics-based resistive switching memories. *Nature Mater.* **6,** 833–840 (2007).
5. Ohno, T. *et al.* Short-term plasticity and long-term potentiation mimicked in single inorganic synapses. *Nature Mater.* **10,** 591–595 (2011).
6. Terabe, K., Hasegawa, T., Nakayama, T. & Aono, M. Quantized conductance atomic switch. *Nature* **433,** 47–50 (2005).
7. Tamura, T. *et al.* Material dependence of switching speed of atomic switches made from silver sulfide and from copper sulfide. *J. Phys. Conf. Ser.* **61,** 1157–1161 (2007).
8. Morales-Masis, M., van der Molen, S. J., Hasegawa, T. & van Ruitenbeek, J. M. Bulk and surface nucleation processes in Ag_2S conductance switches. *Phys. Rev. B* **84,** 115310 (2011).
9. Nayak, A., Tsuruoka, T., Terabe, K., Hasegawa, T. & Aono, M. Switching kinetics of a Cu_2S-based gap-type atomic switch. *Nanotechnology* **22,** 235201 (2011).
10. Nayak, A. *et al.* Rate-limiting processes determining the switching time in a Ag_2S atomic switch. *J. Phys. Chem. Lett.* **1,** 604–608 (2010).
11. Milchev, A., Stoyanov, S. & Kaischev, R. Atomistic theory of electrolytic nucleation: I. *Thin Solid Films* **22,** 255–265 (1974).
12. Budevski, E., Staikov, G. & Lorenz, W. J. *Electrochemical Phase Formation and Growth* (Wiley, 1996).
13. Milchev, A. *Electrocrystallization: Fundamentals of Nucleation and Growth* (Kluwer Academic, 2002).
14. Hebb, M. H. Electrical conductivity of silver sulfide. *J. Chem. Phys.* **20,** 185–190 (1952).
15. Wagner, C. *Proc. 7th Meet. Int. Comm. On Electrochem. Thermodynam. Kinet.* (Butterworths, 1957).
16. Delahay, P. *Double Layer and Electrode Kinetics* (Wiley, 1965).
17. Butler, J. A kinetic theory of reversible oxidation potentials at inert electrodes. *Trans. Faraday Soc.* **19,** 734–739 (1924).
18. Erdey-Gruz, T. & Volmer, M. Zur Theorie der Wasserstoffueberspannung. *Z. Phys. Chem-Leipzig* **150A,** 203–213 (1930).
19. Pinkowski, A., Chierchie, T. & Lorenz, W. Low-temperature ion conductivity of $RbAg_4I_5$. *J. Electroanal. Chem.* **285,** 241–248 (1990).
20. Dovesi, R. *et al.* CRYSTAL09 User's Manual, University of Torino (2010).
21. Bredow, T. & Gerson, A.R. Effect of exchange and correlation on bulk properties of MgO, NiO, and CoO. *Phys. Rev. B* **61,** 5194–5201 (2000).
22. Leininger, T. *et al.* The accuracy of the pseudopotential approximation: Non-frozen-core effects for spectroscopic constants of alkali fluorides XF (X = K, Rb, Cs). *Chem. Phys. Lett.* **255,** 274–280 (1996).
23. Andrae, D., Haeussermann, U., Dolg, M., Stoll, H. & Preuss, H. Energy-adjusted *ab initio* pseudopotentials for the 2nd and 3rd row transition elements. *Theor. Chim. Acta* **77,** 123–141 (1990).
24. Peterson, K. A., Shepler, B. C., Figgen, D. & Stoll, H. On the spectroscopic and thermochemical properties of ClO, BrO, IO, and their anions. *J. Phys. Chem. A* **110,** 13877–13890 (2006).
25. Weigend, F. & Ahlrichs, R. Balanced basis sets of split valence, triple zeta valence and quadruple zeta valence quality for H to Rn: Design and assessment of accuracy. *Phys. Chem. Chem. Phys.* **7,** 3297–3312 (2005).
26. Geller, S. Crystal structure of solid electrolyte $RbAg_4I_5$. *Science* **157,** 310–311 (1967).

Acknowledgements

The authors would like to thank the German Research Foundation (DFG) and the Japan Science and Technology Agency (JST) for the financial support of the projects *WA*908/22-1 in Germany and that in Japan. I.S. was supported by the 'Studienstiftung des deutschen Volkes'. The assistance of T. Pössinger with the graphical layout is gratefully acknowledged.

Author contributions

I.V. conceived the idea, supervised the measurements, performed the data interpretation and wrote the manuscript. I.S. prepared the samples, performed the measurements and the data evaluation, and contributed to the interpretation. A.N. and T.T. supported the STM measurements and contributed to the interpretation. T.B. performed the DFT calculations, T.H. supervised the STM measurements and contributed to the interpretation. G.S. contributed to the interpretation, M.A and R.W. contributed to the concept of the study and supervised the research. All authors discussed the results and implications at all stages and contributed to the improvement of the manuscript text.

Additional information

The authors declare no competing financial interests. Supplementary information accompanies this paper on www.nature.com/naturematerials. Reprints and permissions information is available online at www.nature.com/reprints. Correspondence and requests for materials should be addressed to I.V.